




Multi-field Split Curvature Wavefront Sensing and its Application in the Large Field Survey Telescope

Zhixu Wu¹, Yiming Zhang², Jianan Cong², Hua Bai^{2,3} , Yong Xia¹, Rongxin Tang¹, Ming Li¹, Zhengyang Li², and Xiangyan Yuan^{2,3}

¹ Institute of Space Science and Technology, Nanchang University, Nanchang 330031, China; wuzhixu@ncu.edu.cn

² Nanjing Institute of Astronomical Optics & Technology, CAS, Nanjing 210042, China; ymzhang@niaot.ac.cn, zyli@niaot.ac.cn

³ University of Chinese Academy of Sciences, Nanjing, Nanjing 211135, China; xyyuan@niaot.ac.cn

Received 2024 January 17; revised 2024 April 29; accepted 2024 May 22; published 2024 July 24

Abstract

The image quality of a large field survey telescope with a fast focal ratio of the primary mirror is high sensitivity to the optical elements' misalignments and the primary mirror's deformations. To maintain good optical performance, the perturbations need to be aligned, and the tomographic reconstruction of these perturbations can be derived from wavefront sensing with multi-field points for alignment. This work undertakes a comprehensive examination related to the implementation and optimization of a multi-field split curvature wavefront sensing system, including defocus distance, signal pre-processing, deblending of overlapped doughnuts, field-dependent correction, and distorted coordinate correction. We also conduct experiments to demonstrate the application and performance of a multi-field split curvature wavefront sensing system in Mephisto. In the context of the decentering of the secondary mirror, the coefficient of determination (R) attains a high value of 0.993, indicating a robust linearity between the coma coefficients and the decentering of the secondary mirror. A comparative analysis of the simulated and experimental results shows that the difference between them is less than 0.1λ .

Key words: Instrumentation: high angular resolution – Techniques: photometric – Techniques: image processing

1. Introduction

Over the past two decades, large field survey telescopes have played a pivotal role in addressing a multitude of scientific objectives, such as creating comprehensive sky surveys to aid in the discovery of new astronomical phenomena (Wang 2018), investigating the nature of dark energy and dark matter by observing large-scale structures in the universe (Oguri et al. 2012), studying the evolution and distribution of galaxies to understand their formation and development over cosmic time (Padilla & Strauss 2008) and exploring other critical aspects of astrophysics research.

The imperative for enhanced image quality and higher time frequency in the ever-expanding landscape of scientific research propels the development of the next generation of sky survey telescopes. Within the latest generation of sky survey telescopes, there is a discernible trend toward increasing the aperture of the primary mirror to enhance the light-gathering capabilities. This necessitates the adoption of a fast focus ratio for the primary mirror to minimize the secondary mirror's obscuration and shorten the barrel's length. Exemplary instances, including J-PAS (Cenarro et al. 2018), LSST (Stubbs et al. 2004), Mephisto (Yuan et al. 2020), KDUST (Yuan et al. 2012), and WFST (Lou et al. 2016), are characterized by a primary mirror focal ratio of less than 2. It is a very challenging task to maintain the high performance of this kind of telescope

during the observation, primarily attributed to the heightened sensitivity of image quality to both the misalignment of optical elements and environmentally induced deformations of the primary mirror. Active optics, facilitated by measuring wavefronts at multiple field points, emerges as a viable solution for correcting the misalignments of optical elements and deformations in the primary mirror.

In large field survey telescopes of the new generation, the measurement of wavefronts at multiple field points is predominantly facilitated by split curvature wavefront sensors (Xin et al. 2015; Chueca et al. 2012). Distinguished from the traditional Shack-Hartmann wavefront sensor (SHWFS), the split curvature wavefront sensor offers notable advantages in source selection owing to the large field of view afforded by area sensors. Moreover, SHWFS necessitates placement near the focal plane to avoid vignetting in a fast focal ratio system. This requirement imposes constraints on the dimensions of reimaging optics and micro-lens arrays for effective encapsulation within the CCD's vacuum cavity. In contrast, the split curvature wavefront sensor presents a comparatively uncomplicated configuration, facilitating integration into the CCD panel.

This work undertakes a comprehensive examination related to the implementation and optimization of a multi-field split curvature wavefront sensing system, such as defocus distance,

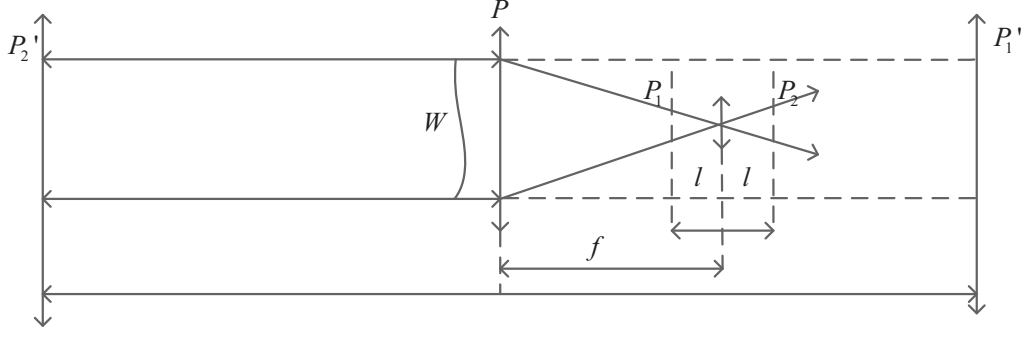


Figure 1. The optical configuration of the curvature wavefront sensor.

Table 1
Curvature Wavefront Sensor for Sky Survey Telescopes

| Telescope | F/# | Implementation of CWFS | DOF of the Perturbations | Field Points | Defocus Length |
|-----------|------|------------------------|--------------------------|--------------|----------------|
| VISTA | 3.6 | Beam splitter | 5 | 2 | 1.2 mm |
| J-PAS | 3.5 | Split CWFS | 7 | 4 | 1 mm |
| DECam | 2.7 | Split CWFS | 5 | 8 | 1.5 mm |
| LSST | 1.23 | Split CWFS | 24 | 4 | 1 mm |
| WFST | 2.48 | Split CWFS | 14 | 4 | 1 mm |

pre-processing of signal sources, the decoupling of signals from neighboring sources, field-dependent corrections, and distorted coordinate correction for intensity compensation. Subsequently, the curvature wavefront sensing system on Mephisto is evaluated through the experiment, and the simulation of active alignment procedures is tested.

2. Principle of Multi-field Split Curvature Wavefront Sensing

2.1. Configuration of the Multi-field Split Curvature Wavefront Sensor

For the traditional curvature sensor, the acquisition of intra-focus and extra-focus images typically involves the use of a beam splitter (Clark et al. 2004) or physically moving the detector (Roddier & Roddier 1993). However, the application of a beam splitter strategy encounters challenges for integrating into the crowded focal plane, as the volume of the beam splitter must increase to avoid the vignetting for the fast beams. Alternatively, the method employing a distorted diffraction grating (Fengjie et al. 2007) or a non-coaxial Fibonacci-sieve filter (Zhang et al. 2019) can capture both intra-focus and extra-focus images in a single-shot. Nevertheless, these elements pose practical design challenges in dealing with sources in random fields. Notably, the split curvature wavefront sensor (CWFS) has gained prevalence in sky survey telescopes, as

detailed in Table 1. The intra- and extra-focal sources of the split CWFS come from two different parts of the field of view, each captured by separate CCDs: one positioned in front of the focus and the other situated behind it.

Multi-field split curvature wavefront sensors are typically positioned at the marginal fields of the focal plane. This strategy not only preserves fields characterized by high image quality for science but also reduces the condition number of the sensitive matrix and enhances the stability of tomographic reconstruction for the perturbations. The scalability of the sensitive matrix's dimension is achieved by augmenting the number of measured field points, offering a more robust solution to the perturbation solving process. Drawing on a simulation conducted by Liang et al. (Liang et al. 2012) for the Large Synoptic Survey Telescope (LSST), a minimum of three curvature wavefront sensors is necessary to ensure the sensitive matrix attains full rank for the calibration of the 24 perturbation parameters (10 rigid body motions and 14 mirror deformations). Furthermore, employing wavefront sensors at four field points proves effective in reducing the condition number of the sensitive matrix.

2.2. Wavefront Estimating Algorithms

In the context of the paraxial approximation, the intensity transport equation (ITE) quantitatively describes the intricate relationship between the wavefront of the beam and intensity variations in light intensity along the optical axis (Streibl 1984). As the optical configuration of the curvature wavefront sensor depicted in Figure 1, under the assumption of a uniformly illuminated pupil with intensity denoted as I_0 , the ITE can be simplified to a Poisson equation with Neumann boundary condition.

$$-\frac{1}{\Delta z} \frac{I_2 - I_1}{I_2 + I_1} \approx \nabla^2 W(\vec{r}) + \delta_c \frac{\partial W(\vec{r})}{\partial n} \quad (1)$$

where f is the focal length, l is the defocus length, $\Delta z = \frac{f(f-l)}{l}$ is the conjugate distance of l , \vec{r} is the coordinate at the pupil

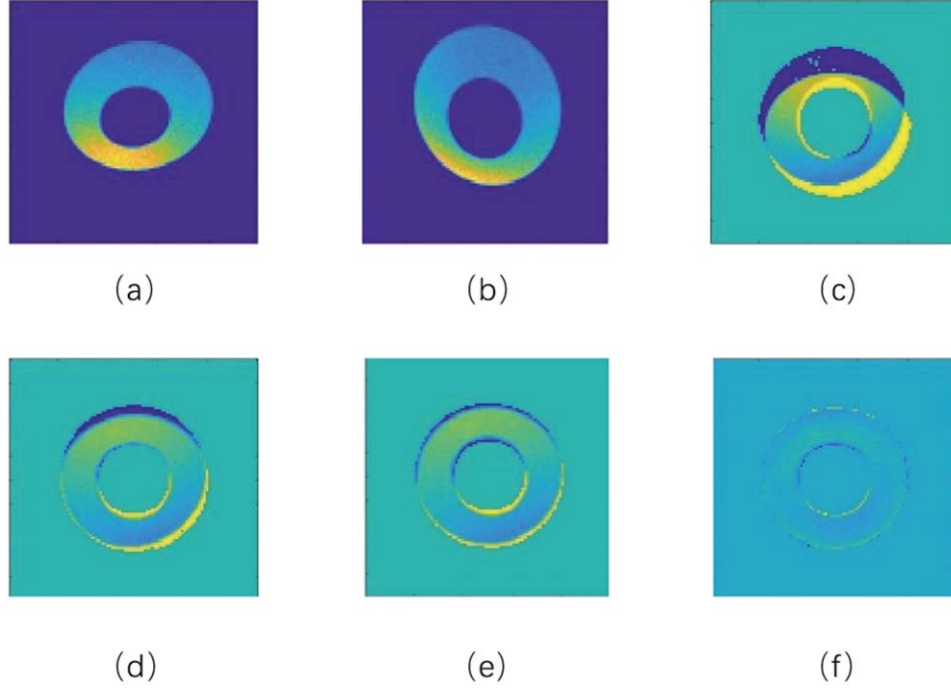


Figure 2. Reconstruction of the wavefront was introduced in the Mephisto. First row: intra-focus image, extra-focus image, curvature signal. Second row: curvature signal after 5, 10, 20 iterations.

Table 2
Examples of Wavefront Reconstruction from Simulated Data

| Zernike Term | Zernike Coefficients(unit: λ) | | | | | | | |
|--------------|--|-------------|---------------|-------------|---------------|-------------|---------------|-------------|
| | Ground Truth1 | Estimated 1 | Ground Truth2 | Estimated 2 | Ground Truth3 | Estimated 3 | Ground Truth4 | Estimated 4 |
| Z4 | 0.574 | 0.563 | 0.204 | 0.204 | 0.204 | 0.196 | 0.052 | 0.054 |
| Z5 | -0.601 | -0.631 | -0.311 | -0.293 | -0.086 | -0.082 | -0.327 | -0.328 |
| Z6 | -1.009 | -1.027 | 0.222 | 0.194 | 0.226 | 0.216 | 0.508 | 0.486 |
| Z7 | -0.680 | -0.579 | 0.830 | 0.790 | 0.676 | 0.651 | 0.112 | 0.118 |
| Z8 | -0.172 | -0.142 | 0.204 | 0.175 | -0.649 | -0.678 | 0.512 | 0.468 |
| Z9 | 0.000 | -0.013 | 0.000 | 0.009 | 0.000 | -0.033 | 0.000 | -0.006 |
| Z10 | 0.000 | 0.014 | 0.000 | -0.017 | 0.000 | 0.038 | 0.000 | 0.006 |
| Z11 | -0.041 | -0.039 | -0.038 | -0.038 | -0.038 | -0.038 | -0.037 | -0.038 |
| Z12 | 0.001 | 0.002 | -0.001 | 0.003 | -0.002 | -0.003 | -0.003 | 0.006 |
| Z13 | 0.002 | -0.006 | 0.001 | 0.001 | 0.001 | -0.002 | 0.001 | 0.001 |
| Z14 | 0.000 | 0.001 | 0.000 | -0.009 | 0.000 | 0.003 | 0.000 | -0.003 |

plane, $I(\vec{r})$ is the illumination distribution inside the pupil, I_1 and I_2 are the intensity of intra- and extra- focal images, $W(\vec{r})$ is the wavefront, ∇^2 is the Laplace operator, \vec{n} is the radial direction of the pupil.

The differentiation of the intensity distribution along the optical axis is directly proportional to the wavefront curvature; therefore, this technology is commonly called a CWFS (Rodier et al. 1988). Various algorithms can be employed to

estimate the wavefront in curvature wavefront sensing, including the Fast Fourier Transform algorithm (FFT) (Rodier et al. 1990), the series expansion method, deep learning (Patterson & Sutherland 2003), etc. For the popular FFT algorithms, the Neumann boundary condition at the pupil edge needs to be absorbed into the Laplace operator by setting the outside intensity equal to the inside intensity along the radial direction \vec{n} , then $\frac{\partial W(\vec{r})}{\partial \vec{n}} = 0$. Apply FFT transform to both sides

of Equation (1),

$$\mathcal{F}\left\{-\frac{1}{\Delta z} \frac{I_2 - I_1}{I_2 + I_1}\right\} = -4\pi^2(\mu^2 + v^2) \cdot \mathcal{F}\{W(\vec{r})\}. \quad (2)$$

The wavefront can be estimated by,

$$W(\vec{r}) = \mathcal{F}^{-1}\left\{\frac{\mathcal{F}\left\{-\frac{1}{\Delta z} \frac{I_2 - I_1}{I_2 + I_1}\right\}}{-4\pi^2(\mu^2 + v^2)}\right\}. \quad (3)$$

As emphasized by Roddier (Roddier & Roddier 1993), the Poisson equation serves as a first-order approximation applicable primarily to small Δz values corresponding to highly defocused images. Furthermore, aberrations must remain sufficiently small to confine the distortion of defocused images within the linear range (Roddier & Roddier 1993). However, in the presence of substantial aberrations, it becomes imperative to enhance accuracy through iterative compensation aimed at compensating the distortion inherent in defocused images. Assuming the system is paraxial, the coordinates (x, y) in the defocus plane is a scaled-down of the normalized coordinates $(x_p/R, y_p/R)$ in the pupil plane, that is $x = lx_p/Rf$ and $y = ly_p/Rf$, where R is the radius of the pupil. An aberration $W(x_p, y_p)$ in the pupil plane will produce coordinate deviation of the rays,

$$\begin{cases} x' = x + C \frac{\partial W(x, y)}{\partial x} \\ y' = y + C \frac{\partial W(x, y)}{\partial y} \end{cases} \quad (4)$$

where $C = -\frac{f(f-l)}{l} \frac{1}{R^2}$. The intensity of point (x', y') and point (x, y) has to satisfy flux conservation,

$$\begin{aligned} I(x, y) = I'(x', y') & \left\{ 1 + C \left(\frac{\partial^2 W}{\partial x^2} + \frac{\partial^2 W}{\partial y^2} \right) \right. \\ & \left. + C^2 \left[\frac{\partial^2 W}{\partial x^2} \frac{\partial^2 W}{\partial y^2} - \left(\frac{\partial^2 W}{\partial xy} \right)^2 \right] \right\}. \end{aligned} \quad (5)$$

The widely employed FFT algorithm, coupled with intensity compensation, has found extensive application in wavefront estimation. In this study, we applied this algorithm to the wavefront reconstruction of Mephisto, subjecting it to extensive testing using simulated defocused images characterized by known low-order aberrations. Figure 2 depicts intra- and extra-focus images simulated through ray tracing of the Geometric Image Analysis in ZEMAX. The curvature signal exhibited diminishing magnitudes as the defocused image intensities were compensated iteratively by the estimated aberrations. After 20 iterations, discernible signals became negligible. Across all cases outlined in Table 2, wavefront

reconstruction consistently yielded errors below 5%. The efficacy of the algorithm was further evaluated on the real Mephisto telescope, with performance details provided in Section 4.2.

3. Implementation of Multi-field Split Curvature Wavefront Sensing

3.1. The Defocus Distance

The defocus distance emerges as a pivotal parameter in configuring multi-field split Curvature wavefront Sensing. With an increase in defocus distance, the doughnut-shaped images occupy a larger pixel area, concurrently diminishing the signal-to-noise ratio (S/N) and elevating the likelihood of blending in sky regions with dense stellar objects. Additionally, the intensity patterns of defocused images become less sensitive to the wavefront, a consequence of reduced Fisher information (Fienup et al. 1998). The advantages conducive to curvature wavefront sensing include the weakening of atmospheric turbulence effects on the doughnut-shaped images and an enhancement in the adequacy of pupil sampling.

Recognition of the wavefront error through the algorithm is contingent upon distorted coordinates of the ray deviation exceeding 1 pixel, that is,

$$x' - x = C \cdot \frac{\partial W}{\partial x} > 1\text{pixel} \text{ or } y' - y = C \cdot \frac{\partial W}{\partial y} > 1\text{pixel}. \quad (6)$$

Expand the wavefront error in terms of Zernike polynomials,

$$\frac{\partial W}{\partial x} = \sum_i zc_i \frac{\partial Z_i}{\partial x} \quad \text{and} \quad \frac{\partial W}{\partial y} = \sum_i zc_i \frac{\partial Z_i}{\partial y}. \quad (7)$$

Here zc_i is the Zernike coefficient, Z_i is the i th Zernike polynomial. By analyzing the partial derivatives expression of the Zernike polynomials in Table 3, $\max \left\{ \left| \frac{\partial Z_i}{\partial x} \right| | p = r \right\}$ and $\max \left\{ \left| \frac{\partial Z_i}{\partial y} \right| | p = r \right\}$ at different pupil position r can be calculated (shown in Figure 3). To enable sufficient data for the wavefront reconstruction, we take the number of recognizable pixels to be greater than half and take the pupil radius of 0.4 as a reference. Assuming a wavefront reconstruction accuracy of 0.01λ , then $Z_4(p = 0.4) \approx 0.48$, the upper limit of defocus distance should be,

$$l \leq \frac{4\left(\frac{f}{d}\right)^2 \cdot 0.01\lambda \cdot 0.48}{1 \text{ pixel}}. \quad (8)$$

On the other hand, the defocus images of CWFS must stay away from the caustic zone to avoid the intensity patterns smeared by the blurred point-spread function. For the observatory site to have Kolmogorov spectrum with Fried

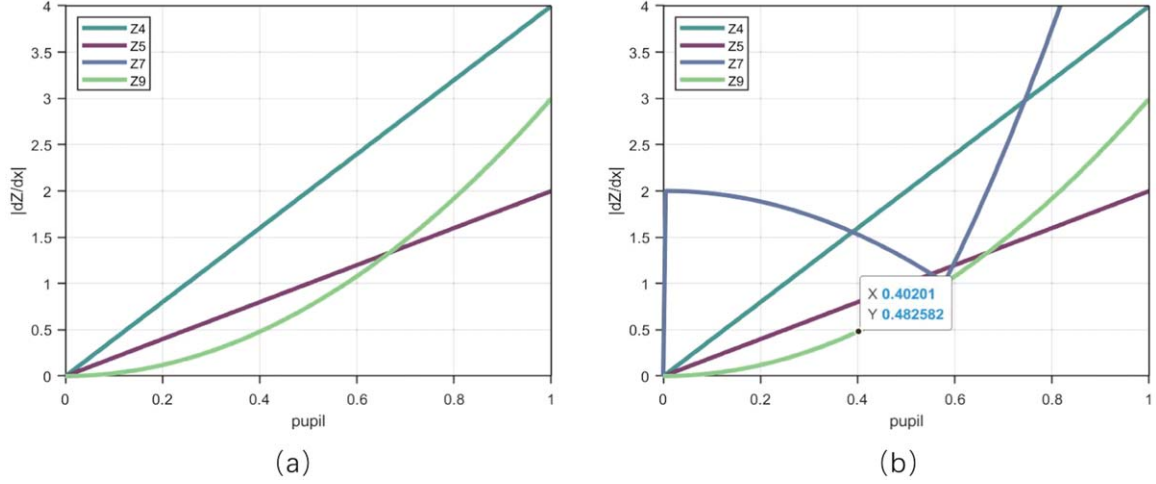


Figure 3. (a) $\max \left\{ \left| \frac{\partial Z_i}{\partial x} \right| \right\}$ at different pupil size; (b) $\max \left\{ \left| \frac{\partial Z_i}{\partial y} \right| \right\}$ at different pupil size.

Table 3
The Partial Derivatives Expression of the Zernike Polynomials

| Polynomials Number | Expression | Z_x | Z_y |
|--------------------|-----------------------|-------------------|-------------------|
| Z4 | $(x^2 + y^2) - 1$ | $4x$ | $4y$ |
| Z5 | $2y$ | $2y$ | $2x$ |
| Z6 | $x^2 - y^2$ | $2x$ | $-2y$ |
| Z7 | $[3(x^2 + y^2) - 2]$ | $6xy$ | $3x^2 + 9y^2 - 2$ |
| Z8 | $x[3(x^2 + y^2) - 2]$ | $9x^2 + 3y^2 - 2$ | $6xy$ |
| Z9 | $y(3x^2 - y^2)$ | $6xy$ | $3(x^2 - y^2)$ |
| Z10 | $x(x^2 - 3y^2)$ | $3(x^2 - y^2)$ | $-6xy$ |

parameter r_0 , the defocused distance l must satisfy (Rod-dier 1988):

$$\frac{\lambda f^2}{r_0^2} \ll l. \quad (9)$$

For example, for the system with parameters of $D=2$ m, $f=4$ m, $\lambda=0.5 \mu\text{m}$, $1\text{pixel}=15 \mu\text{m}$, $r_0=10$ cm, the range of the defocus distance would be,

$$0.2 \text{ mm} \ll l \leq 4 \text{ mm}. \quad (10)$$

3.2. Signal Pre-processing and Deblending

In the context of simulated defocused images depicted in Figure 4(a), multi-field split curvature wavefront sensors capture a bunch of doughnuts simultaneously. To isolate optimal doughnuts, the initial step involves binarising the intensity pattern of these doughnuts, as represented by the false color in Figure 4(a), through the application of a threshold. The

threshold value is determined using the OTSU algorithm. Subsequently, the doughnuts in the binarised image are subjected to segmentation and labeling based on connected area analysis. Here, the connected area pertains to a region in the image characterized by identical values in a 4- or 8-neighborhood of the pixel. Figure 4(c) presents the segmented doughnuts with different colors denoting distinct tagged values. By utilizing this segmentation approach, doughnuts with a specific S/N can be readily identified and selected.

Due to the expansion of the point source into doughnuts consisting of hundreds of pixels, there is an increased probability of blending between two adjacent doughnuts in densely sky regions. Figure 5(a) illustrates this phenomenon, where doughnut images from fainter stars overlay the target doughnut, introducing background noise. To mitigate the impact of fainter doughnuts on the curvature signal, it is imperative to eliminate the intensity contribution of fainter doughnuts in the overlapping regions. To achieve this, we initially employ the Sobel operator to detect edges in the blended image. Subsequently, the blended image is segmented into distinct regions based on these edges. By labeling these segmented regions, we can accurately identify and extract the intensity of the fainter doughnut in non-overlapping areas, fitting the data to polynomials as depicted in Figure 5(c). In areas of overlap, the background noise originating from the fainter doughnut can be estimated and removed through the application of the fitted intensity distribution. Figure 5(d) presents the deblended target doughnut, with iterative processes contributing to enhanced deblending accuracy.

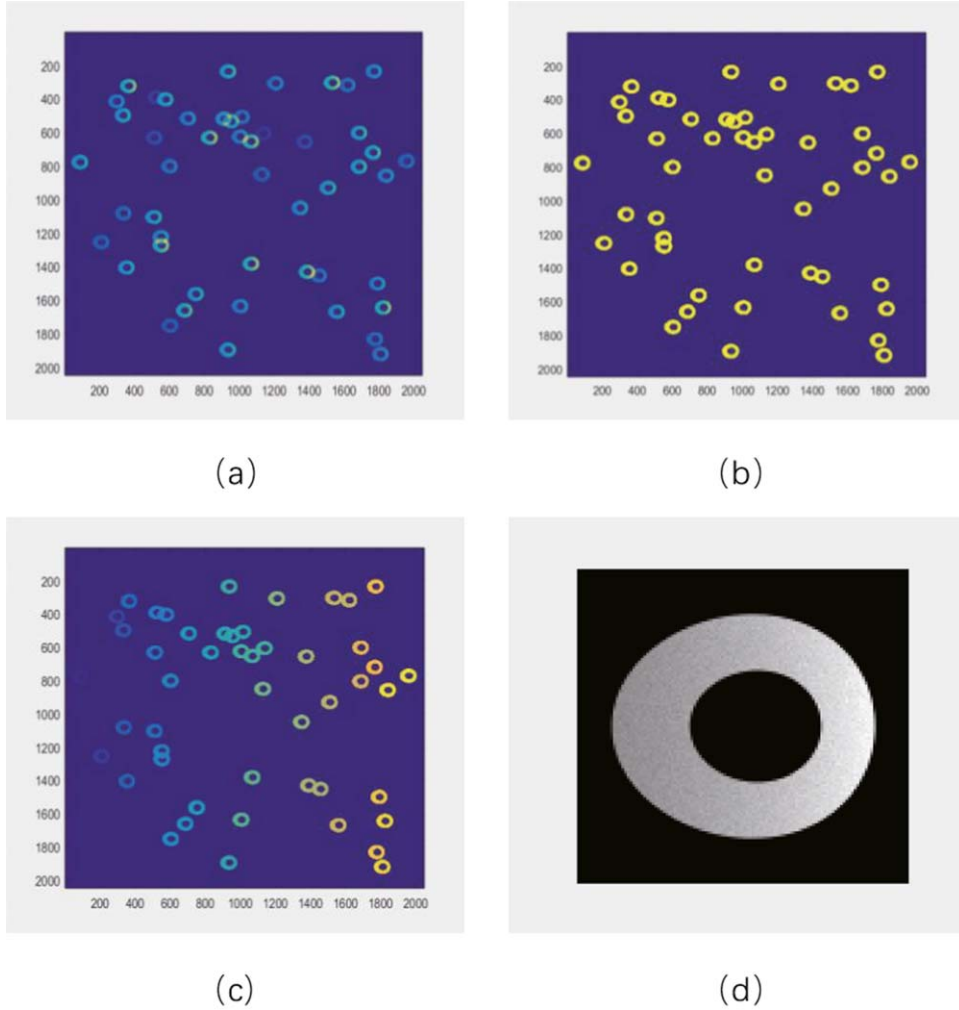


Figure 4. (a) Image of the simulated defocus CCD; (b) the binarised image (c) the labeled doughnuts of the image; (d) the picked out doughnut.

3.3. Field-dependent Corrections

For the split CWFS, the curvature signal is derived from intra- and extra-focal doughnuts originating from different stars, each possessing non-identical optical properties.

In these optical properties, the intensity difference can be effectively overcome by normalization. Furthermore, the intra- and extra-focal doughnuts, sourced from different regions of CWFS, inherently exhibit non-common path aberrations and variations in pupil geometry due to distinct beam footprints (Xin et al. 2015). Compensation is applied to mitigate the impact of non-common path aberrations by addressing the intrinsic design aberrations. Figure 6 illustrates the Zernike coefficients representing these intrinsic design aberrations across the curvature wavefront sensor field for Mephisto. By using the center field of the curvature wavefront sensor as a reference, non-common path aberrations can be subtracted

through intensity compensation. This results in the migration of doughnuts from different fields to the center field of CWFS.

3.4. Coordinate Correction for the Intensity Compensation

As described in Sections 2.2 and 3.3, both the iterative FFT and the series expansion algorithm for solving the Poisson equation with Neumann boundary conditions represent first-order solutions. Enhancing estimation accuracy is achievable through the integration of the intensity compensation algorithm. This algorithm assumes a pivotal role not only in ameliorating the inherent limitations of the first-order solutions but also in compensating for non-identical optical properties pertinent to Field-Dependent Corrections. Our previous work has expounded upon the correction of nonlinear coordinate distortion arising from fast-beam optical properties and off-axis

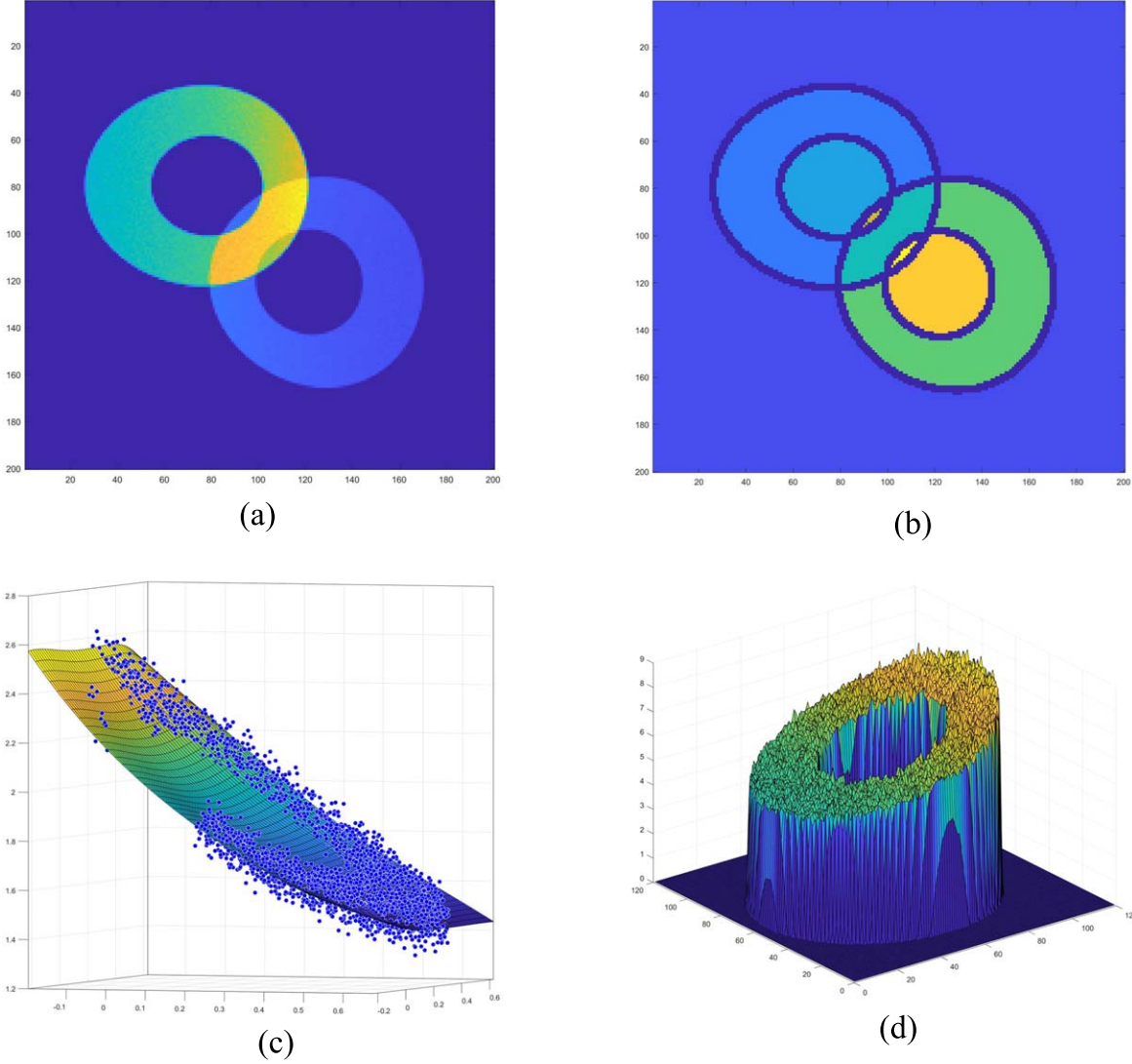


Figure 5. (a) The blended doughnuts of two neighborhood signals; (b) the segmented regions; (c) the polynomial fit of the non-overlapping area; (d) the deblended target doughnut.

effects (Wu et al. 2015). Figure 7 describes the coordinate distortion of fast-beam and off-axis mode.

$$\begin{cases} x' = D_1(x, y) + C \frac{\partial W(x, y)}{\partial x} \\ y' = D_2(x, y) + C \frac{\partial W(x, y)}{\partial y} \end{cases} \quad (11)$$

where $\begin{cases} D_1(x, y) = \frac{f}{\sqrt{f^2 - (x^2 + y^2) \cdot R^2}} \cdot x \\ D_2(x, y) = \frac{f}{\sqrt{f^2 - (x^2 + y^2) \cdot R^2}} \cdot y \end{cases}$ for the on-axis fast-beam system and $\begin{cases} D_1(x, y) = \frac{f}{\sqrt{f^2 - (x^2 + y^2) \cdot R^2}} \cdot \frac{1}{\cos \beta - \sin \beta \cdot \cos \beta \frac{y \cdot R}{f}} \cdot x \\ D_2(x, y) = \frac{f}{\sqrt{f^2 - (x^2 + y^2) \cdot R^2}} \cdot \frac{1}{\cos \alpha - \sin \alpha \cdot \cos \alpha \frac{y \cdot R}{f}} \cdot y \end{cases}$ for the off-axis fast-beam system.

Bo Xin et al. (Xin et al. 2015) introduced a more comprehensive approach through numerical mapping, transitioning from the pupil ($x - y$ plane) to the intra- and extra-focal images ($x' - y'$ plane). In this method, a set of 10th-order two-dimensional polynomials accurately delineates the relationship between the two coordinate sets. This generalized numerical mapping provides a more precise depiction of the nonlinear and non-axisymmetric projection inherent to a specific optical system. Using Mephisto as an illustration, we calculate the distorted coordinates for the fast-beam mode and off-axis mode using both analytical and numerical methods. Figure 8 illustrates the comparability of distorted coordinates derived from these two methodologies, indicating a high degree of similarity.

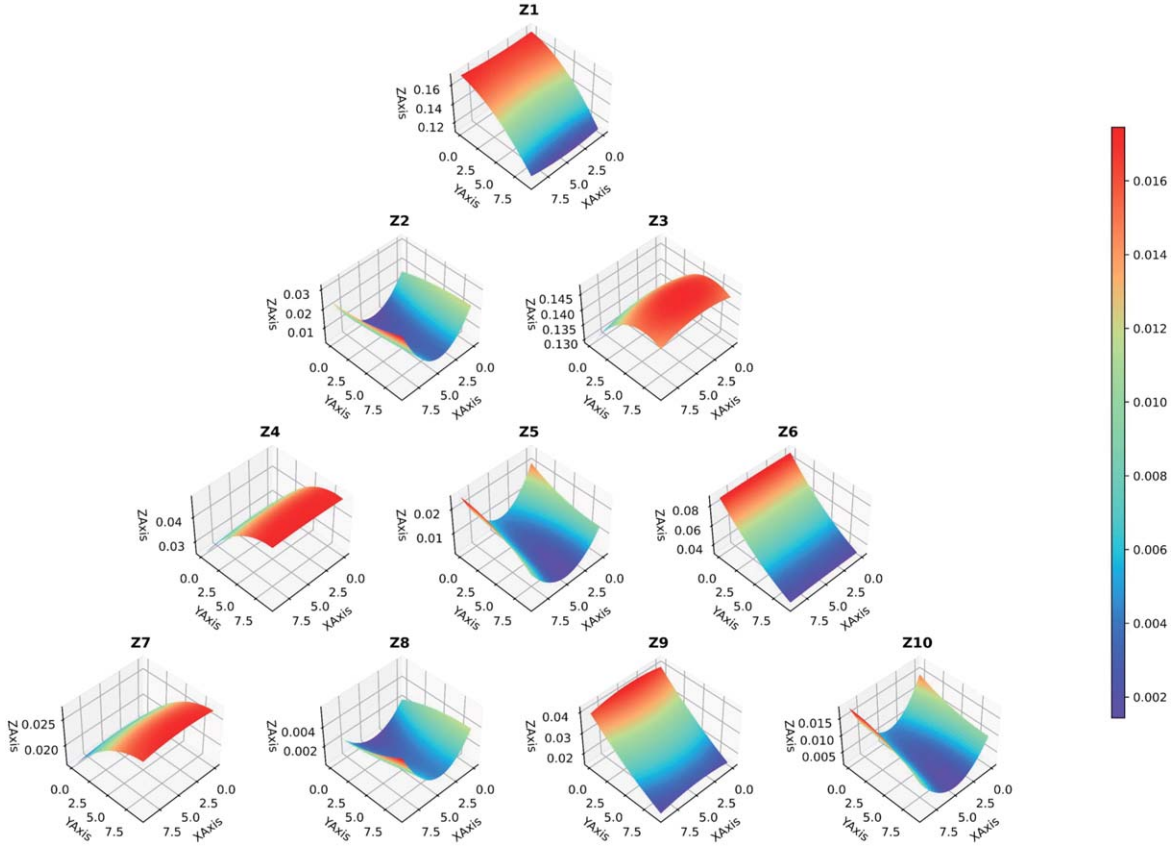


Figure 6. Zernike coefficients distribution of the non-common path aberrations.

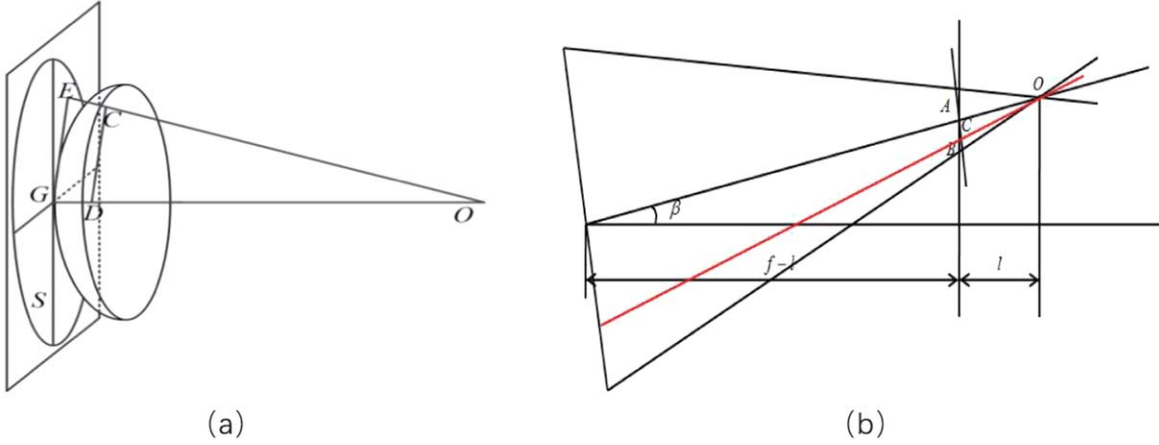


Figure 7. The coordinate distortion of (a) fast-beam mode and (b) off-axis mode.

4. Multi-field Split CWFS for Mephisto

4.1. Optical Configuration of Mephisto

Multi-channel Photometric Survey Telescope (Mephisto) is a large field ground-based telescope with a 1.6 m primary mirror

and 2° field of view (Liu 2019). Figure 9 describes the optical layout of Mephisto, three films coated cubic prisms were adopted for delivering a 3-channel colored movie of the universe. This innovative approach enables the telescope to provide real-time, high-precision colors for celestial objects,

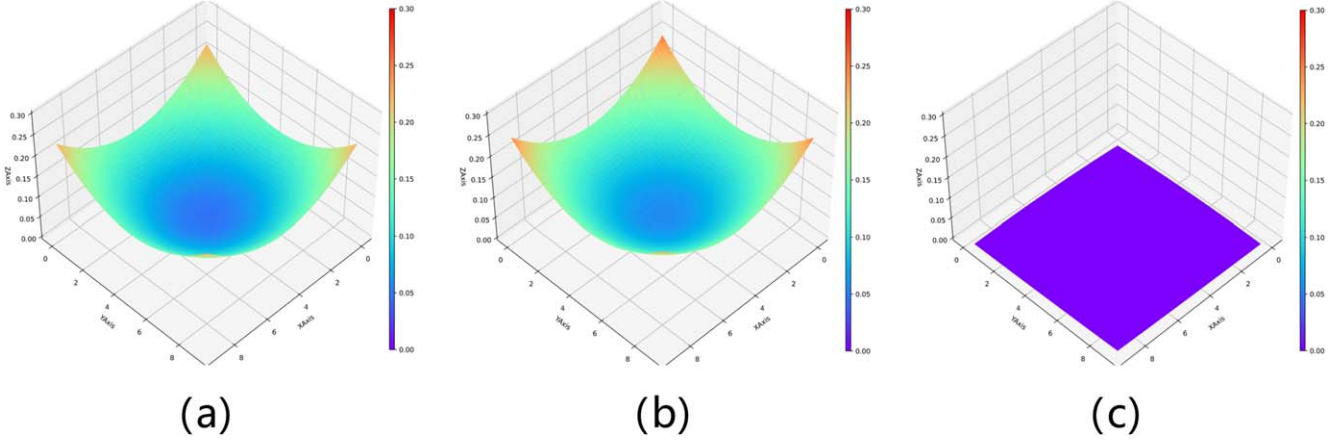


Figure 8. Nonlinear coordinate mapping of the pupil to defocus plane. (a) Analytic mapping; (b) numerical mapping; (c) the difference between the two methods.

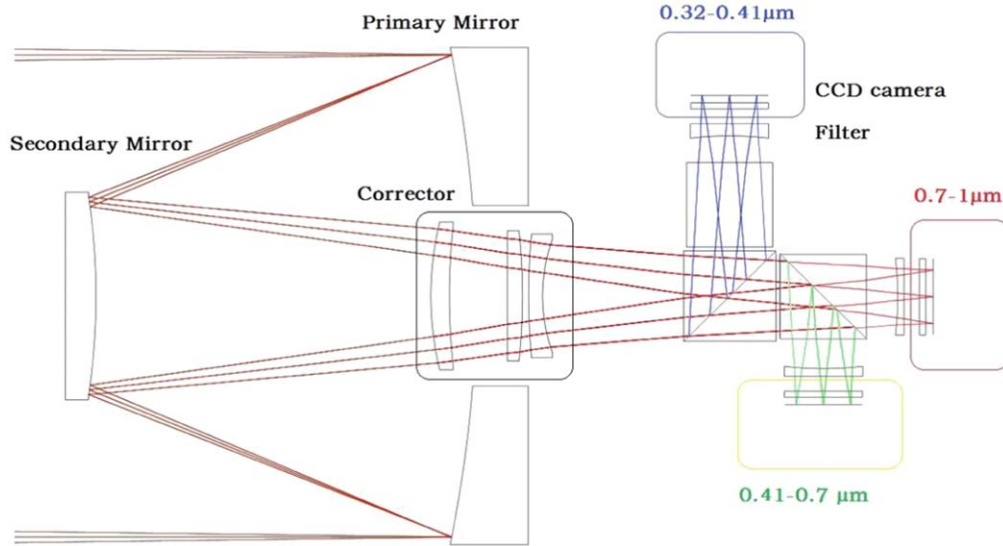


Figure 9. Optical layout of Mephisto.

fostering rapid and robust classification of variables and transients. Mephisto's capabilities extend to delivering panoramic and panchromatic documentation of our evolving universe, marking a significant advancement in observational astronomy.

Driven by considerations encompassing image quality requirements, light obscuration, and focal instruments assignment, the Ritchey-Chretien (RC) optical system, augmented with a lens corrector, has been chosen for Mephisto. The 0.7 m secondary mirror of Mephisto proves to be notably sensitive to alignment adjustments, owing to the fast focal ratio of the primary mirror. The field-dependent image quality of misaligned Mephisto optics manifests as asymmetric, continuously varying, and nonlinear with the misalignments. To address this challenge, a 5-degree-of-freedom (DOF) mechanism has been designed to actively adjust M2 mirror positions based on

feedback from the multi-field wavefront sensor. This adaptive mechanism ensures optimal image quality under operational conditions. It is noteworthy that the compact configuration of Mephisto allows for a mere 15mm distance between the focal plane and the last optical surface. In such a crowded space, the CWFS stands out for its ease of installation in comparison to the SHWFS, especially in crowded spaces.

4.2. First Light for CWFS on Mephisto

Mephisto is being built by NIAOT and installed at Lijiang Gaomeigu Observatory ($100^{\circ}2' \text{ E}$, $26^{\circ} 42' \text{ N}$, 3200 m). On 2023 June 16, experimental tests of the curvature wavefront sensor were conducted. System aberrations were diligently minimized, and the camera was positioned at the plane

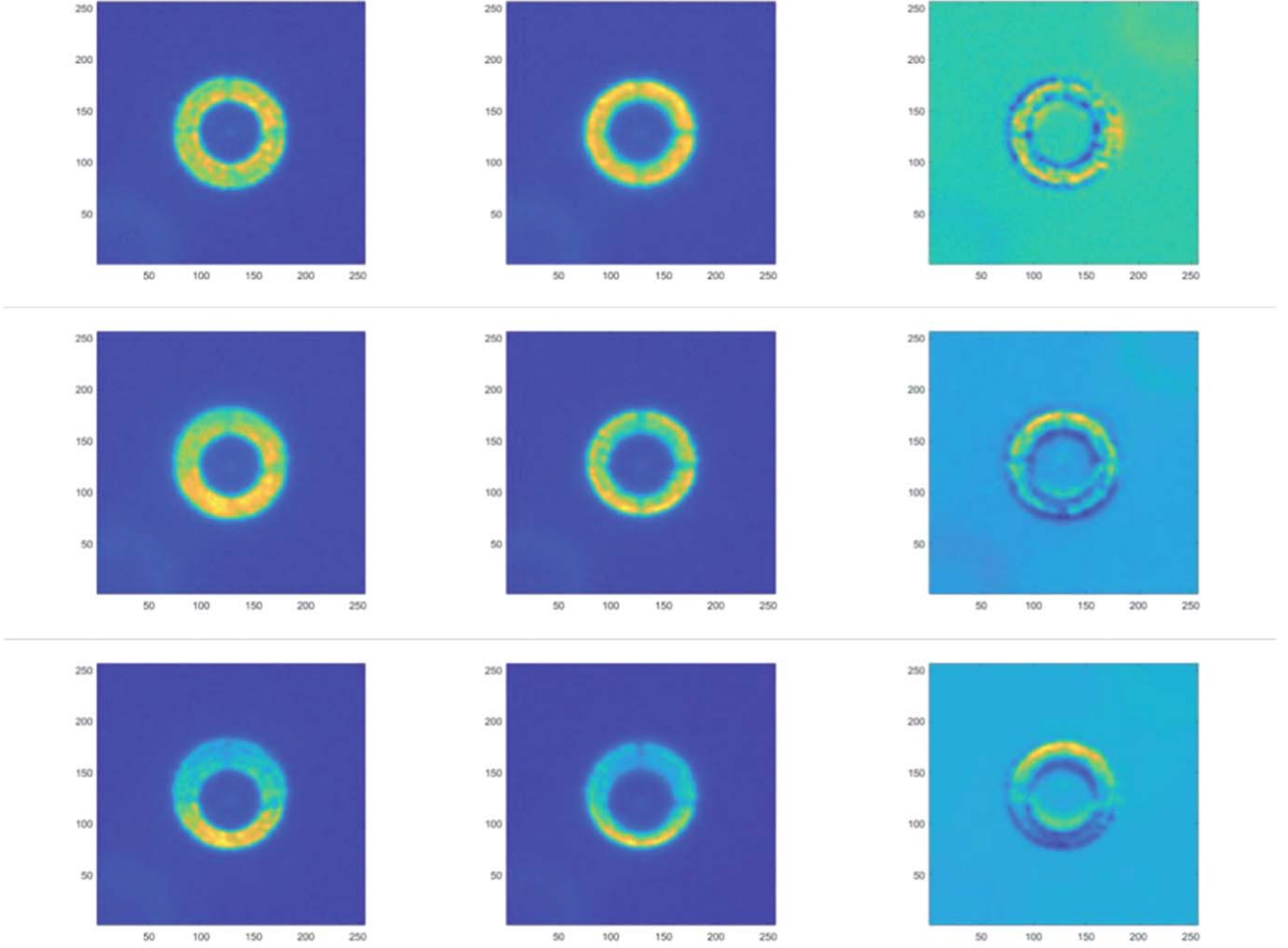


Figure 10. Linearly increase of the introduced coma term in the Mephisto. From left to right: intra-focus image, extra-focus image, curvature signal; From top to bottom: decent $x = 0$ mm, decent $x = 0.08$ mm, decent $x = 0.2$ mm.

corresponding to the best focal plane with minimum stellar images. Because the signal area with about 50×50 pixels has relatively better wavefront sensing results, the intra- and extra-defocus images were systematically captured by displacing the secondary mirror 0.28 mm along the optical axis, effectively simulating a defocused distance of 3.4 mm. Employing ray tracing of Mephisto, a linear increase in the decentering of the secondary mirror introduced an indicated coma value. The series of defocus images, illustrated in Figure 10, portray the evolving impact of increased decentering of the secondary mirror, progressing from 0 mm to 0.08 mm and 0.2 mm. The first two columns present the intra-focus and extra-focus images, and the third column depicts the curvature signal (S). Evidently, the intensity accumulates toward the bottom of the defocus images with an increase in the decenter x of the secondary mirror, concurrently indicating an increase in the coma.

The wavefront is estimated collectively by the inner iteration of the Poisson equation solver and the outer iteration of intensity compensation. To assess the effectiveness of curvature wavefront sensing, an examination of the linearity between coma coefficients and the decentering of the secondary mirror is conducted. Figure 11 illustrates the variation in estimated Zernike coefficients corresponding to the increasing decentering of the secondary mirror along the x -direction. The coefficient of determination serves as a quantitative measure of linearity,

$$R^2 = 1 - \frac{\sum_{i=1}^n (y_i - \hat{y}_i)^2}{\sum_{i=1}^n (y_i - \bar{y}_i)^2}. \quad (12)$$

Where y_i is the Z7 coefficients, \hat{y}_i is the fitted value, \bar{y}_i is the mean value of y_i , n is the sample size. The coefficient of determination (R) for Z7 attains a high value of 0.993, indicating a strong correlation and affirming the robust linearity

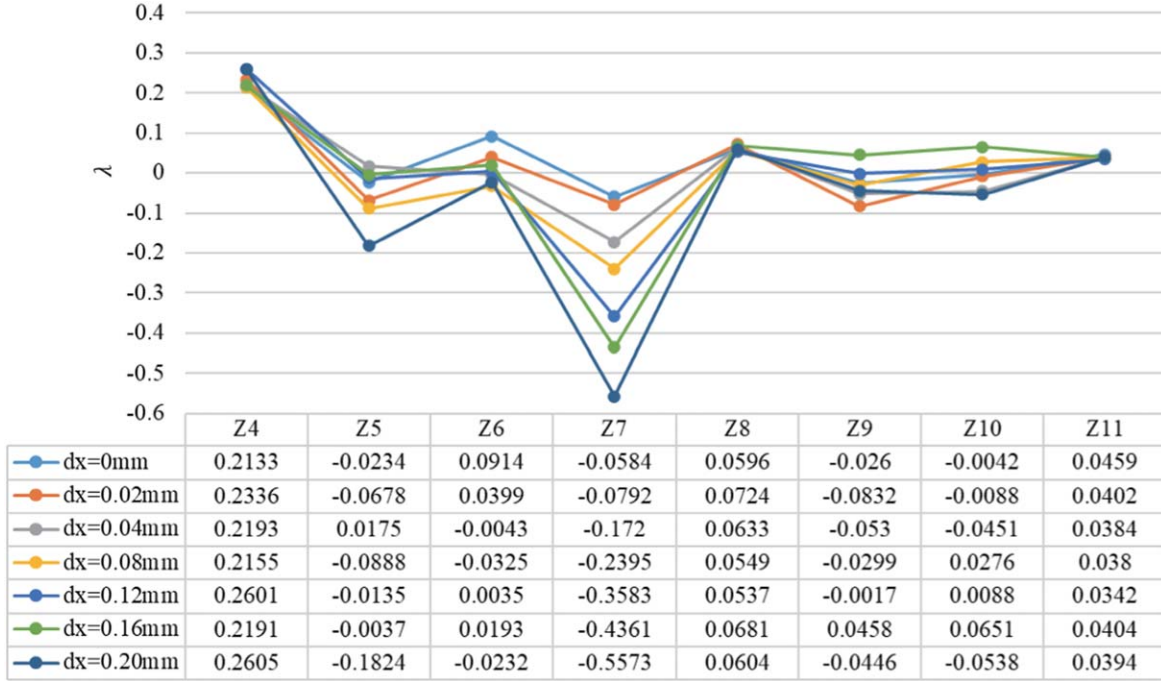
Figure 11. The estimated Zernike coefficients with different decenter x .

Table 4
The Partial Derivatives Expression of the Zernike Polynomials

| Iteration | Misalignment Parameters | | | | | | | |
|------------|-------------------------|-----------------------|------------------------|------------------------|-----------------------|-----------------------|------------------------|------------------------|
| | M2 Piston (mm) | M2 Decenter x (mm) | M2 Decenter y (mm) | M2 Tilt x (°) | M2 Tilt y (°) | CCD piston (mm) | CCD Tilt x (°) | CCD Tilt y (°) |
| Introduced | 2 | 2 | 0 | 0.02 | 0.02 | 0 | 0.02 | 0.02 |
| Estimate | | | | | | | | |
| 1 | 1.27×10^{-3} | 1.74×10^{-3} | -2.47×10^{-3} | -1.42×10^{-4} | 1.52×10^{-4} | 3.43×10^{-3} | -1.91×10^{-4} | 3.04×10^{-4} |
| 2 | 2.34×10^{-7} | 6.89×10^{-7} | 7.17×10^{-7} | -8.40×10^{-8} | 8.3×10^{-8} | 6.37×10^{-7} | 2.65×10^{-7} | -2.50×10^{-7} |

between the Z7 coefficients and the decentering of the secondary mirror along the x -direction. Notably, the Z7 term demonstrates linear enlargement, while the Z8 term consistently remains small, confirming their decoupled nature. Consequently, decentering in the x -direction does not influence the Z8 term. The Z4 term stabilizes within the range of 0.21–0.26, indicating a slight offset of the telescope focus from the optimal position. Additional confirmation of the linearity between Z7 coefficients and decentering in the x -direction is presented in Figure 12(a). The difference between the simulated and experimental results, as depicted by the error bars measuring less than 0.1λ . The oscillation observed in the astigmatism terms Z5 and Z6 can be attributed to the slight tilt

of the secondary mirror. Figure 12(b) presents an additional set of measurements involving a decentered secondary mirror in both the x and y directions. Notably, a discernible linearity is observed in the Z7 terms concerning decentering in the x -direction and the Z8 term in relation to decentering in the y -direction. Figure 13 is a comparison between the theoretical adjustment amount of the secondary mirror and the actual measurement value.

We introduced an unknown decentering to the secondary mirror, subsequently measuring the coma aberration through the curvature wavefront sensor. With the linear relationship depicted in Figure 12, the decentering value of the secondary mirror is determined and corrected. As shown in Figure 14,

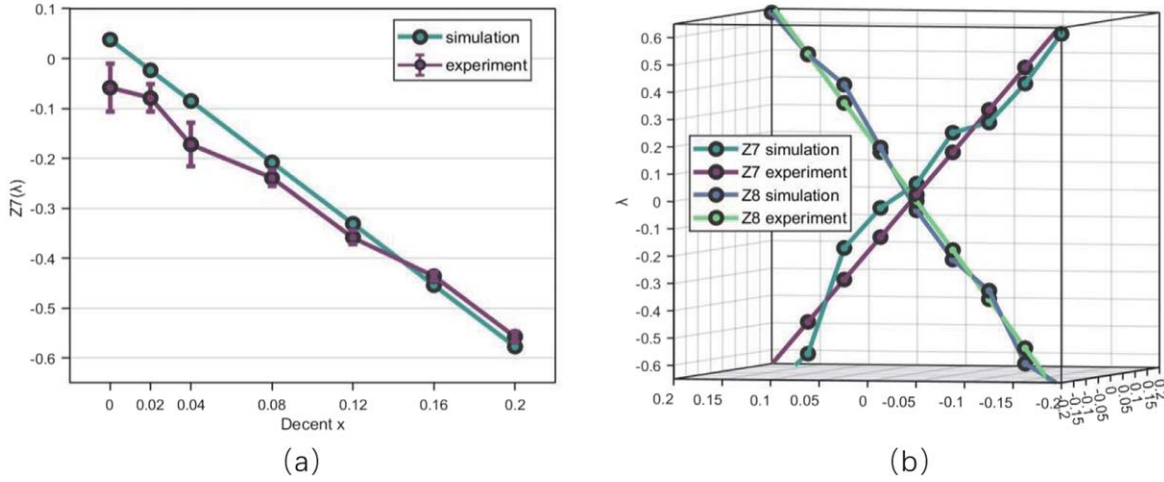


Figure 12. (a) The linearity of Z7 as the decenter x increases; (b) the linearity of Z7 and Z8 as decenter x and decenter y increases.

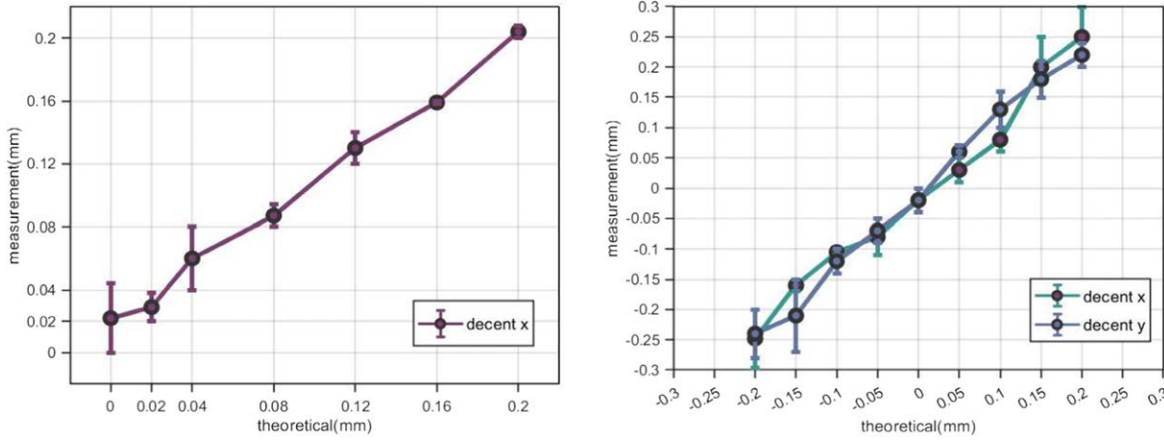


Figure 13. Comparison of theoretical adjustment and the actual measurement.

even with large fluctuations of the seeing and incomplete calibration of other misalignments (FWHM about $2''$), the images captured after introducing the decentering of the secondary mirror exhibit noticeable coma aberration. After correction, the coma aberration has been effectively mitigated.

4.3. Performance of Active Alignment for Mephisto

An application has been specifically developed for Mephisto, with the user interface (UI) showcased in Figure 15. Within this software, four fundamental modules are defined:

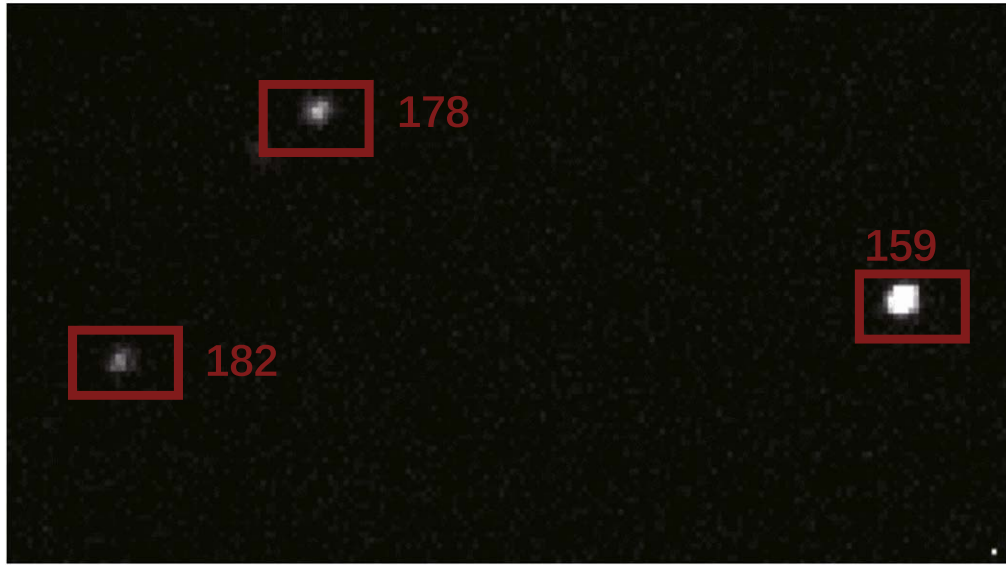
1. *CWFS Control*: This module facilitates the configuration of parameters related to the CWFS, encompassing optical characteristics of Mephisto (diameter, focal length, obscuration), CCD parameters (pixel size, pixel number), and defocus distance.

2. *Source Selector*: This module enables the selection of source signals for the wavefront sensors and calculates the field associated with each signal.
3. *Wavefront Estimator*: Source signals are transposed from their original field positions to the central field position of the CWFS. Subsequently, the wavefront is estimated through the inner iteration of the Poisson equation solver and the outer iteration of compensating for estimated aberrations.
4. *Misalignment Calculator*: This module determines the rigid body motions of the second mirror and the focal plane through a sensitivity matrix.

The fundamental functions of the first three modules have been illustrated in Section 3. Here is a comprehensive description of Module 4. The relationship between misalignments and wavefront errors of each field point can be



(a)



(b)

Figure 14. (a) The image captured after introducing the decenter of the secondary mirror; (b) the image captured after correction of the decenter of the secondary mirror.

represented by,

$$\begin{bmatrix} F_1 \\ F_2 \\ \vdots \\ F_m \end{bmatrix} = \begin{bmatrix} f_1(x_1, x_2, \dots, x_n) \\ f_2(x_1, x_2, \dots, x_n) \\ \vdots \\ f_m(x_1, x_2, \dots, x_n) \end{bmatrix} + \begin{bmatrix} F_{01} \\ F_{02} \\ \vdots \\ F_{0m} \end{bmatrix}. \quad (13)$$

Here F_j is the Zernike coefficients of wavefront errors at each field point, F_{0j} is the baseline design aberrations, function f_j characterizes the asymmetric, continuous varying and nonlinear

relationship, x_j is the misalignment parameters. Finding an exact expression for f_j proves to be challenging; nevertheless, f_j can be effectively approximated through linear equations, particularly when subjected to minor misalignments.

$$F_j = F_{0j} + \frac{\partial f_j}{\partial x_1}(x_1 - x_{01}) + \frac{\partial f_j}{\partial x_2}(x_2 - x_{02}) + \dots + \frac{\partial f_j}{\partial x_n}(x_n - x_{0n}), \quad (14)$$

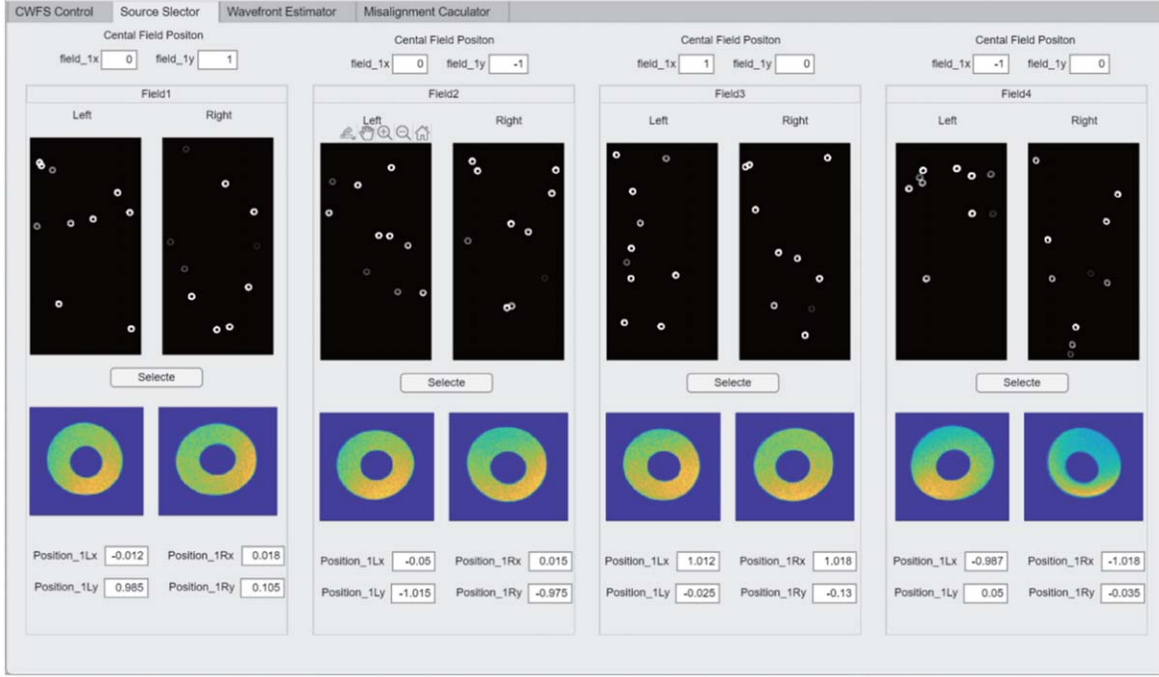


Figure 15. The UI of the active optics for Mephisto.

where $\frac{\partial f_j}{\partial x_i}$ is the partial derivative of the Zernike aberration f_j to the misalignment parameter x_i , which can be approximated as difference equations,

$$F_j = F_{0j} + \frac{\partial f_j}{\partial x_1}(x_1 - x_{01}) + \frac{\partial f_j}{\partial x_2}(x_2 - x_{02}) + \dots + \frac{\partial f_j}{\partial x_n}(x_n - x_{0n}). \quad (15)$$

Then the approximate linear equations for aberration and misalignment are,

$$\begin{bmatrix} F_1 - F_{01} \\ F_2 - F_{02} \\ \vdots \\ F_m - F_{0m} \end{bmatrix} = \begin{bmatrix} \frac{\partial f_1}{\partial x_1} & \frac{\partial f_1}{\partial x_2} & \dots & \frac{\partial f_1}{\partial x_n} \\ \frac{\partial f_2}{\partial x_1} & \frac{\partial f_2}{\partial x_2} & \dots & \frac{\partial f_2}{\partial x_n} \\ \vdots & \vdots & \ddots & \vdots \\ \frac{\partial f_m}{\partial x_1} & \frac{\partial f_m}{\partial x_2} & \dots & \frac{\partial f_m}{\partial x_n} \end{bmatrix} \cdot \begin{bmatrix} x_1 - x_{01} \\ x_2 - x_{02} \\ \vdots \\ x_n - x_{0n} \end{bmatrix}. \quad (16)$$

Represent the equations in matrix,

$$\Delta F = S \cdot \Delta x \quad (17)$$

where ΔF is the deviation of the measured aberration from the designed aberration, Δx is the value of each misalignment parameter, S is the sensitive matrix.

S is typically computed by numerically introducing perturbations with specific step lengths ($\Delta x_1, \Delta x_2, \dots, \Delta x_n$) into the

optical system. The choice of step length for each perturbation is contingent upon its sensitivity, a metric assessable through the eigenvalues of S . Perturbations characterized by larger eigenvalues, such as tilt- x and tilt- y of the second mirror, indicate a heightened sensitivity, necessitating smaller step lengths to confine aberrations within the linear range. Conversely, less sensitive perturbations, like the tilt- x and tilt- y of the camera, require larger step lengths to ensure the magnitude of aberration changes surpasses wavefront sensing errors.

The misalignment parameters Δx can be solved from the measure wavefront errors,

$$\Delta x = (S^T S)^{-1} S^T \Delta F. \quad (18)$$

In this study, the strategy employed for simulating active alignment involves utilizing Dynamic Data Exchange (DDE) between ZEMAX and MATLAB. Perturbation values are generated through MATLAB and subsequently transferred to ZEMAX. The wavefront errors for each field point are then determined through ray tracing and conveyed to MATLAB for the calculation of the sensitive matrix and compensator signals. The retrieved misalignment parameters from simulated data are presented in Table 4. Perturbations corresponding to the rigid body motion of the second mirror (M2) and CCD are introduced with their respective values outlined in Table 4. Importantly, the remaining perturbations after a single iteration fall within the tolerances defined for the telescope.

5. Conclusions

This work presents a comprehensive analysis of the multi-field split curvature wavefront sensing system. The upper limit of the defocus distance is determined based on the distorted coordinates of ray deviation. The labeling of doughnuts from various sources involves an initial categorization by connected areas, facilitating the subsequent selection of optimal signals. For deblending overlapped doughnuts from neighboring sources within the blended image, different segment regions are defined. The non-overlapping areas of fainter doughnuts are subjected to polynomial fitting, and overlapping areas are estimated and removed through these fitted polynomials. Compensation for non-identical optical properties between intra- and extra-focal images is implemented. Both analytical and numerical methods are employed to calculate distorted coordinates for fast-beam and off-axis modes, with a subsequent comparative analysis of the results.

The curvature wavefront sensor was effectively tested on Mephisto, demonstrating its capability to diagnose telescope aberrations accurately. Specifically, we conducted tests focusing on the prevalent coma aberrations arising from the decentering of the second mirror. The observed coma exhibited consistent linearity with the incremental decentering of the second mirror. Furthermore, simulations were performed to assess the active alignment performance of Mephisto, yielding retrieved misalignment parameters from simulated data that fall within the defined tolerances for the telescope.

Acknowledgments

This work was supported by the National Natural Science Foundation of China (grant No. 12173062). The authors would like to thank SWIFAR (South-Western Institute for Astronomy

Research, Yunnan University) and YNAO (Yunnan Observatories, Chinese Academy of Sciences) for the defocused image acquisition of Mephisto.

ORCID iDs

Hua Bai  <https://orcid.org/0000-0002-9641-7227>

References

- Cenarro, A., Ederoclite, A., Íñiguez, C., et al. 2018, *Proc. SPIE*, 10700, 93
- Chueca, S., Marín-Franch, A., Cenarro, A. J., et al. 2012, *Proc. SPIE*, 8450, 173
- Clark, P., Berry, P., Bingham, R. G., et al. 2004, *Proc. SPIE*, 5499, 379
- Fengjie, X., Zongfu, J., Xiaojun, X., & Yifeng, G. 2007, *JOSAA*, 24, 3444
- Fienup, J. R., Thelen, B. J., Paxman, R. G., & Carrara, D. A. 1998, *Proc. SPIE*, 3353, 940
- Liang, M., Krabbendam, V., Claver, C. F., Chandrasekharan, S., & Xin, B. 2012, *Proc. SPIE*, 8444, 1524
- Liu, X. 2019, in Electronic Proc. of “Galactic Archaeology in the Gaia Era” (*Sexten Center for Astrophysics (SCfA)*)
- Lou, Z., Liang, M., Yao, D., et al. 2016, *Proc. SPIE*, 10154, 587
- Oguri, M., Inada, N., Strauss, M. A., et al. 2012, *AJ*, 143, 120
- Padilla, N. D., & Strauss, M. A. 2008, *MNRAS*, 388, 1321
- Patterson, B. A., & Sutherland, W. J. 2003, *Proc. SPIE*, 4842, 231
- Roddier, C. A., Roddier, F. J., Stockton, A. N., Pickles, A. J., & Roddier, N. A. 1990, *Proc. SPIE*, 1236, 756
- Roddier, C., & Roddier, F. 1993, *JOSAA*, 10, 2277
- Roddier, F. 1988, *ApOpt*, 27, 1223
- Roddier, F., Roddier, C., & Roddier, N. 1988, *Proc. SPIE*, 976, 203
- Streibl, N. 1984, *OptCo*, 49, 6
- Stubbs, C. W., Sweeney, D., Tyson, J. & LSST Collaboration 2004, AAS Meeting, 205, 108.02
- Wang, L. 2018, *China’s e-Science Blue Book* (Singapore: Springer), 85
- Wu, Z.-X., Bai, H., & Cui, X.-Q. 2015, *RAA*, 15, 764
- Xin, B., Claver, C., Liang, M., et al. 2015, *ApOpt*, 54, 9045
- Yuan, X., Cui, X., & Su, D.-q. 2012, in Proc. Int. Astron. Union, 271
- Yuan, X., Li, Z., Liu, X., et al. 2020, *Proc. SPIE*, 11445, 1372
- Zhang, X., Zhang, Y., Zhang, J., Yang, P., & Zhu, J. 2019, *ApPhL*, 115, 274